Applied Acoustics 254 (2026) 111486

Contents lists available at ScienceDirect

Applied Acoustics

journal homepage: www.elsevier.com/locate/apacoust

The seismic camera method for water leak pinpointing

P.H.M.C. Matos [a,1], N. Uchendu [a], F.C.L. Almeida [b], M.J. Brennan [b], B.C. Campos [b], M. Karimi [c], J.M. Muggleton [d], E. Rustighi [a,*]

[a] Department of Industrial Engineering, University of Trento, Trento, Italy
[b] Department of Mechanical Engineering, UNESP, Bauru, Sao Paulo 15385-000, Brazil
[c] Centre for Audio, Acoustics and Vibration, University of Technology Sydney, Sydney, Australia
[d] Institute of Sound and Vibration Research (ISVR), University of Southampton, Southampton SO17 1BJ, United Kingdom

ARTICLE INFO

Keywords:
Beamforming
Array signal processing
Seismic analysis
Water leak
Pinpointing

ABSTRACT

Water leakages in buried plastic pipelines pose significant challenges due to high wave attenuation, which limits the effectiveness of conventional acoustic detection methods. A widely used approach relies on the cross-correlation of leak noise signals measured at two distinct positions along the pipeline to estimate the time delay and infer the leak location from pipe vibration data. In practice, the method may become unreliable when the propagation velocity of the leak noise or the time delay is poorly estimated, which frequently occurs in plastic pipes and heterogeneous soils. To assist correlation-based surveys, this paper presents a non-invasive leak pinpointing technique termed the Seismic Camera Method (SCM). The approach uses a mobile array of ground-mounted vibration sensors combined with beamforming and seismic wave analysis to generate real-time visual maps that guide users to the leak location. The method accurately estimates the direction of arrival (DOA) of leak-induced body waves propagating to the ground surface, thereby transforming the sensor array into a directional imaging tool. Depth averaging and summing over multiple frequency bands are used to reduce errors due to grating lobes, ensuring robust leak pinpointing performance. Numerical simulations and experimental validations demonstrate that the approach reliably converges on the leak location despite uncertainties in wave speed and soil properties. The proposed methodology demonstrates the feasibility of the seismic camera concept for supporting leak surveys in plastic water distribution systems, indicating its potential to reduce search area and perhaps inspection time.

1. Introduction

Leakage in water distribution systems remains a critical global challenge, with annual losses estimated at 126 billion m^3 and associated costs of about 39 billion US dollars [1]. Considerable research effort has therefore been directed towards the development of reliable leak detection and localisation techniques, spanning acoustic methods [2], transient-based approaches [3], and data-driven and hybrid sensing strategies [4]. Among these, acoustic methods based on leak noise correlation remain one of the most widely used approaches for leak pinpointing [5]. In this method, the time delay between signals recorded at two spatially separated sensors is estimated and combined with an assumed propagation velocity to infer the leak position. However, performance is strongly dependent on signal coherence, accurate knowledge of wave speed, and suitable sensor placement. These requirements are particularly restrictive in plastic pipes, which are increasingly used in modern water distribution networks [6]. Compared with metallic pipes, plastic pipes exhibit higher attenuation, stronger fluid–structure–soil coupling, and increased dispersion, all of which significantly reduce the effective sensing range and degrade correlation-based time-delay estimation [7–10]. To address these limitations, a range of improvements to acoustic leak pinpointing has been proposed. These include cross-correlation shaping [11], the differentiation process [12], and more advanced approaches based on wavelet and data-adaptive techniques [13], cepstral analysis [14], and cross-spectral phase methods [15], as well as multipath identification techniques [16], which enable simultaneous estimation of leak location and wave speed. Despite these developments, acoustic methods remain fundamentally limited by their reliance on pipe-borne or fluid-borne signals, which are highly sensitive to attenuation, environmental noise, and uncertain

* Corresponding author.
E-mail address: emiliano.rustighi@unitn.it (E. Rustighi).

[1] This work was initiated prior to the passing of P.H.M.C. Matos.

https://doi.org/10.1016/j.apacoust.2026.111486
Received 17 April 2026; Received in revised form 16 July 2026; Accepted 19 July 2026
Available online 23 July 2026
0003-682X/© 2026 The Author(s). Published by Elsevier Ltd. This is an open access article under the CC BY-NC-ND license (http://creativecommons.org/licenses/by-nc-nd/4.0/).

propagation conditions.

An alternative perspective is to exploit the fact that leak-induced disturbances are not confined to the pipe system but also radiate into the surrounding soil, where they propagate as elastic waves and can be detected at the ground surface [17,18]. This enables non-invasive measurement using ground vibration sensors such as geophones. In this context, array-based signal processing methods, particularly beamforming, provide a natural framework for estimating the direction of arrival (DOA) of wavefields from spatially distributed measurements [19,20]. Beamforming has been successfully applied in related areas such as structural health monitoring [21] and pipeline systems [22,23], demonstrating its capability for source localisation in complex environments.

However, its direct application to buried water pipe leak pinpointing remains challenging. The wavefield generated by a leak in soil is inherently complex, consisting of mixed wave types and near-field effects, and is strongly influenced by soil heterogeneity and ambient noise [24]. Conventional beamforming formulations typically assume simplified propagation conditions, including homogeneous media and well-defined wave speeds, and their performance degrades when these assumptions are violated. In addition, practical limitations on array aperture and sensor spacing introduce spatial aliasing and restrict usable frequency ranges, further complicating reliable DOA estimation. Alternative non-invasive approaches have also been explored. Acoustic emission techniques using ultrasonic sensor arrays can improve spatial resolution but are difficult to scale in field conditions due to coupling and alignment constraints [25]. Surface-based seismic imaging approaches have been proposed for mapping ground vibrations but often neglect the coupled pipe–soil interaction mechanisms that govern leak radiation [26]. Despite advances in robust beamforming for reverberant and noisy environments [27,28], its adaptation to buried pipeline leak localisation remains limited, particularly in the presence of mixed wavefields and uncertain propagation characteristics.

To address these challenges, this paper introduces the Seismic Camera Method (SCM), a non-invasive leak pinpointing approach based on iterative DOA estimation using a roving array of ground vibration sensors. Unlike conventional acoustic methods, SCM does not require access to the pipe or precise prior knowledge of wave speed. Instead, pinpointing is achieved through directional guidance, whereby beamforming estimates are used to iteratively reposition the sensor array until convergence to the leak location. The proposed framework incorporates two key signal processing strategies to improve robustness. First, frequency summing is employed to stabilise DOA estimates by reducing incoherent and frequency-dependent artefacts. Second, depth averaging is introduced to account for the vertical distribution of wave energy in the soil. The performance of the method is systematically evaluated using a simplified finite element model of a buried medium-density polyethylene (MDPE) pipe, enabling controlled analysis of frequency dependence and wave-speed uncertainty. Experimental validation on a buried pipe test rig further demonstrates that the method can reliably localise leaks despite uncertainty in propagation conditions, thereby bridging numerical predictions with practical applicability.

This work presents SCM as a proof-of-concept for leak pinpointing in buried plastic pipes, with the primary objective of establishing feasibility rather than providing a comprehensive treatment of field conditions. The numerical and experimental results are therefore obtained under simplified assumptions, including homogeneous soil and an idealised monopole source, so that the core principles of iterative DOA estimation and robustness to wave-speed uncertainty can be assessed in isolation. A simple square-array configuration and conventional beamforming framework were adopted to demonstrate the leak pinpointing concept without introducing additional complexity associated with array-design optimisation or advanced signal-processing strategies. Although the results are encouraging, extension to practical water networks will require further work on soil anisotropy, variable leak dynamics, optimised array configurations, and environmental noise, which lie beyond the scope of this initial investigation.

The paper is structured as follows: Section 2 introduces the SCM framework, detailing wave propagation mechanisms and the fundamentals of beamforming. Section 3 presents a parametric analysis of critical operational parameters using numerical simulations, while Section 4 provides experimental validation of the method, demonstrating its potential as a scalable, non-invasive leak pinpointing tool. The results are discussed in Section 5, and the main conclusions are presented in Section 6.

2. Seismic camera method for water leak pinpointing

This section introduces the basic principles underlying the operation of the SCM, including wave propagation mechanisms in buried plastic pipes and the surrounding medium, beamforming techniques, and procedures for pinpointing leaks.

2.1. Wave propagation in leaking buried pipes

Understanding wave propagation in leaking buried pipes and the surrounding medium is fundamental to interpreting leak-induced vibrations and enabling reliable detection. Fig. 1 illustrates the main propagation mechanisms. A leak generates localised pressure fluctuations within the pressurised fluid, which propagate as longitudinal acoustic waves along the fluid column and pipe wall, and as body waves in the surrounding soil.

The transmission of energy into the soil occurs through two primary mechanisms [17]: direct radiation from the leak and radiation from the vibrating pipe wall. These mechanisms correspond to different spatial propagation regimes. In the near field of the leak, i.e. in regions close to the leak, body waves propagate directly from the source into the surrounding soil. These waves are predominantly compressional and exhibit approximately spherical wavefronts. At larger distances from the leak, the response transitions to the far field, where the contribution from the vibrating pipe becomes more significant. In this regime, both compressional (P) and shear (S) body waves propagate with well-defined directions and conical wavefronts. Additionally, at lateral offsets from the pipe axis comparable to the burial depth, incident body waves can generate surface waves and reflected bulk waves due to interactions with the ground surface and subsurface interfaces [29,30]. As a result, the measured vibration field at the surface is generally a superposition of multiple wave types and propagation paths.

The scattering of body waves is controlled by the acoustic impedance mismatch at the pipe-soil interface and the difference in wave speeds between the two media [10]. A significant impedance mismatch tends to confine energy within the pipe, whereas a smaller mismatch allows more energy to be radiated into the soil. Similarly, energy is efficiently transmitted into the soil as compressional/shear body waves and surface waves, only when the wave speed in the pipe exceeds that in the soil. Otherwise, the resulting waves in the soil are evanescent, decaying exponentially with radial distance rather than propagating outward. The compressional wave speed c_{p} and shear wave speed c_{s} in a homogeneous, isotropic soil are given by [10].

$$c_{\mathrm{p}} = \sqrt{\frac{B_{\mathrm{soil}} + 4G_{\mathrm{soil}}/3}{\rho_{\mathrm{soil}}}}\ \text{and}\ c_{\mathrm{s}} = \sqrt{\frac{G_{\mathrm{soil}}}{\rho_{\mathrm{soil}}}} \tag{1}$$

where G_{soil}, B_{soil}, and ρ_{soil} are, respectively, the shear modulus, bulk modulus, and density of the soil. The far-field P- and S-waves impinge on the ground surface at angles of incidence ϕ_{p} and ϕ_{s}, respectively [17]:

$$\phi_{\mathrm{p}} = \arccos\left(\frac{c_{\mathrm{p}}}{c_0}\right)\ \text{and}\ \phi_{\mathrm{s}} = \arccos\left(\frac{c_{\mathrm{s}}}{c_0}\right) \tag{2}$$

where c_0 is the pipe acoustic wave speed given by [10]

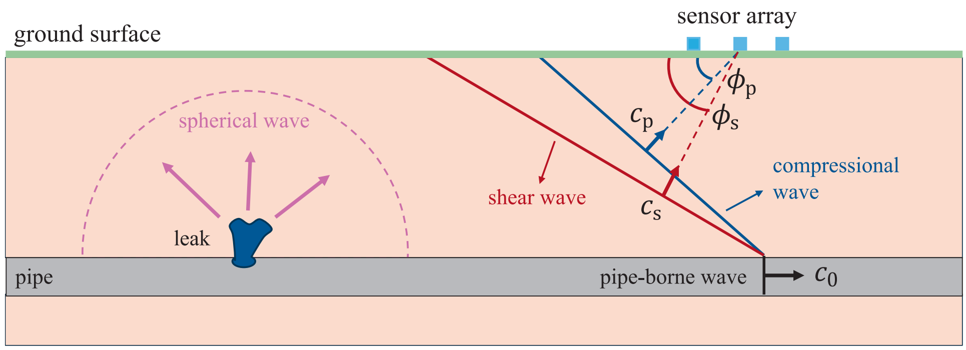

Fig. 1. Schematic of wave propagation in soil surrounding a leaking buried water pipe, illustrating leak-induced body waves and pipe vibrations.

$$c_0 = c_{water}\sqrt{1+\frac{1}{\frac{E_{pipe}h_{pipe}}{2B_{water}a_{pipe}}+\frac{G_{soil}}{B_{water}}}} \quad (3)$$

where E_{pipe}, h_{pipe}, and a_{pipe} are, respectively, the Young's modulus, pipe-wall thickness, and radius of the pipe; $c_{water} = 1500$ m/s is the speed of sound in water; and $B_{water} = 2.2$ GPa is the bulk modulus of water. Soil type and stiffness also affect the wave propagation behaviour: well-compacted, stiff soils transmit body waves more effectively than loose or water-saturated soils. For example, sandy soils support both compressional and shear waves, while saturated clays attenuate shear waves due to their low stiffness and viscoelastic damping [31]. Burial depth influences radiation patterns, so that, shallower burial depths promote the direct radiation of spherical waves detectable at the surface, whereas greater burial depths tend to confine energy along the pipe before it radiates conically into the soil.

As mentioned in the introduction, the detection of leak-induced seismic waves on the ground surface offers a significant potential for detecting and locating leaks. The directional attributes of these waves can be exploited to estimate the leak location. Beamforming techniques for estimating DOA of source signals are described in the following subsection.

2.2. Conventional beamforming for source localisation

Beamforming, a spatial filtering technique that utilises sensor arrays, enhances directional signal reception or transmission by combining sensor signals to constructively reinforce waves from specific directions while destructively suppressing others. This method is widely used in fields such as radar, sonar, seismology, wireless communications, radio astronomy, acoustics, audio applications, and medical imaging [32,33].

The simplest form of beamforming is the conventional or delay-and-sum beamformer [20], which works by aligning or steering the signals temporally or spectrally to enhance coherence from a target direction. Steering the beamformer involves applying time delays (in the time domain) or phase shifts (in the frequency domain) that correspond to the desired direction, leveraging the spatial distribution of the sensors in the array to resolve source signal DOA and/or source locations. The adjusted signals are then summed, enhancing the target direction while suppressing others. The fundamental operation of the receiver delay-and-sum beamformer is described as follows. Consider a sensor array consisting of M sensors, where the sensor is positioned at the coordinates $\mathbf{r}_m = (x_m, y_m, z_m)$ for $m = 1, 2, \cdots, M$. Suppose a source located at $\mathbf{r}_0 = (x_0, y_0, z_0)$ emits a signal $s(t)$. Then, the signal $g_m(t)$ measured by the m-th sensor can be expressed as:

$$g_m(t) = a(t) \otimes s(t-\tau_m) + n_m(t) \quad (4)$$

where $s(t)$ is the source signal, $a(t)$ denotes attenuation effects, $\otimes$ denotes convolution, $n_m(t)$ represents noise at the m-th sensor, $\tau_m = \frac{\|r_m - r_0\|}{c}$ is the time delay between the source and the received signals, c is the speed of wave in the medium, and $\|\mathbf{r}_m - \mathbf{r}_0\| = \sqrt{(x_m-x_0)^2 + (y_m-y_0)^2 + (z_m-z_0)^2}$ is the Euclidean distance between the source and the sensor. The relative delays in the sensor signals will depend on the direction from which the signal arrives at the sensor array. The delay-and-sum beamformer determines the DOA or source location by systematically scanning all potential source locations within a predefined grid and evaluating the power of the time-aligned and summed signals at each grid node/point. For each hypothetical source location $\mathbf{r}_p = (x_p, y_p, z_p)$ within the grid, sensor signals are temporally aligned by applying delays $\tilde{\tau}_{mp} = -\frac{\|\mathbf{r}_m - \mathbf{r}_p\|}{c}$, summed and normalised by the number of sensors to yield the beamformer output given by:

$$\begin{aligned} P(t, x_p, y_p, z_p) &= \frac{1}{M}\sum_{m=1}^{M} w_m g_m(t - \tilde{\tau}_{mp}) \\ &= \frac{1}{M}\sum_{m=1}^{M} w_m g_m\left(t - \frac{\|\mathbf{r}_m - \mathbf{r}_p\|}{c}\right) \end{aligned} \quad (5)$$

where w_m are weights (usually set to 1) that adjust individual sensor signal contributions. Constructive interference amplifies the output power when $\mathbf{r}_p$ aligns with the true source location $\mathbf{r}_0$, while phase mismatches at other grid points result in lower beamformer output levels. This procedure generates a source power map, where the peak value corresponds to the most probable source location.

While this time-domain approach is straightforward, it lacks the flexibility to incorporate optimisation techniques as effectively as frequency-domain beamforming. The frequency-domain beamformer output is given by:

$$P(\omega, x_p, y_p, z_p) = \frac{1}{M}\sum_{m=1}^{M} W_m(\omega)\alpha_m(\omega, x_p, y_p, z_p) G_m(\omega) \quad (6)$$

where $G_m(\omega)$ is the Fourier transform of $g_m(t)$, $W_m(\omega)$ is the frequency-domain weight (typically set to unity for conventional beamforming), and $\alpha_m(\omega, x_p, y_p, z_p)$ is the steering function for the m-th sensor

$$\alpha_m(\omega, x_p, y_p, z_p) = \exp\{\text{-j}\omega\tilde{\tau}_{mp}\} = \frac{1}{\|\mathbf{r}_m - \mathbf{r}_p\|}\exp\{\text{-j}k\|\mathbf{r}_m - \mathbf{r}_p\|\} \quad (7)$$

where $\omega = 2\pi f$ is the angular frequency (f is the frequency), $k = \frac{\omega}{c}$ is the wavenumber, and $\mathrm{j} = \sqrt{-1}$ is the imaginary unit. The beamformer output in Eq. (6) can be implemented in a more computationally convenient and efficient form in terms of the cross-spectral matrix:

$$\hat{\mathbf{R}}(\omega) = \mathbf{G}(\omega)\mathbf{G}^{\mathrm{H}}(\omega) = \begin{bmatrix} G_1(\omega)\,G_1^{\mathrm{H}}(\omega) & \cdots & G_1(\omega)\,G_M^{\mathrm{H}}(\omega) \\ \vdots & \ddots & \vdots \\ G_M(\omega)\,G_1^{\mathrm{H}}(\omega) & \cdots & G_M(\omega)\,G_M^{\mathrm{H}}(\omega) \end{bmatrix} \quad (8)$$

as

$$P\left(\omega,x_p,y_p,z_p\right) = \boldsymbol{\alpha}^{\mathsf{H}}\left(\omega,x_p,y_p,z_p\right)\mathbf{W}^{\mathsf{H}}(\omega)\widehat{\mathbf{R}}(\boldsymbol{\omega})\mathbf{W}(\omega)\boldsymbol{\alpha}\left(\omega,x_p,y_p,z_p\right) \quad (9)$$

where $\boldsymbol{W}_{\text{diag}}(\omega)$ is a diagonal matrix formed from the frequency-domain weights, and the steering vector $\boldsymbol{\alpha}\left(\omega,x_p,y_p,z_p\right) = \begin{bmatrix} \alpha_1\left(\omega,x_p,y_p,z_p\right) \\ \alpha_2\left(\omega,x_p,y_p,z_p\right) \\ \vdots \\ \alpha_M\left(\omega,x_p,y_p,z_p\right) \end{bmatrix}$ encapsulates the relative phase shifts across the array for a signal arriving from the location $\mathbf{r}_p$ within the grid. The superscript H denotes the conjugate transpose. Diagonal removal, which sets the diagonal elements of the cross-spectral matrix to zero to suppress incoherent noise, is usually applied to the cross-spectral matrix to improve the beamforming output [34]. The quantity $P\left(\omega,x_p,y_p,z_p\right)$ can be interpreted as the relative power of the source signal at frequency ω at the array position if the source were located at $\mathbf{r}_p$. Hence, the grid point $\mathbf{r}_s = (x_s, y_s, z_s)$ that maximises the beamformer output provides an estimate of the source location. Alternatively, the DOA of the source signal can be described, relative to the array centre $\mathbf{r}_c = (x_c, y_c, z_c)$, by two angles: the azimuth angle $\phi = \arctan\left(\frac{y_s-y_c}{x_s-x_c}\right)$, measured in the horizontal plane between a reference axis (e.g., the x-axis) and the projection of the source direction onto that plane, and the zenith angle $\theta = \arccos\left(\frac{z_s-z_c}{\|\boldsymbol{r}_s-\boldsymbol{r}_c\|}\right)$, measured from the positive vertical axis to the source direction.

The frequency-domain formulation described above applies only to narrowband signals, where the bandwidth is a small fraction of the centre frequency. Beamforming for wideband signals is performed by dividing them into narrowband frequency bins, each processed independently, and then combining the results to produce the final beamformer output [19]. This allows frequency-specific optimisation of the steering vector, enabling improved representation of wave propagation effects and greater flexibility in selecting analysis frequencies to application needs. The factors that affect beamforming performance are discussed in the following subsection.

2.3. Factors affecting conventional beamforming performance

Beamforming performance is governed by the interplay between array geometry, spatial sampling, signal characteristics, and the chosen processing strategy. The directional response of an array is described by its beampattern, which comprises a main lobe in the look direction and side lobes corresponding to unwanted sensitivity to signals from other directions [20]. Narrow main lobes improve angular resolution, whereas low side-lobe levels reduce interference and false detections. Beampattern characteristics—main-lobe width (beamwidth) and side-lobe levels—together with inter-sensor coherence directly constrain practical performance [35].

Because a sensor array samples the wavefield in space, its design is subject to a spatial analogue of the Nyquist sampling theorem. If the inter-element spacing d exceeds half the wavelength, spatial aliasing occurs, resulting in grating lobes, which are additional beampattern maxima that can be mistaken for the true source direction [19]. For far-field plane waves, a standard requirement is $d \le \frac{\lambda_{min}}{2}$, where λ_{min} corresponds to the shortest wavelength of interest [20]. At low frequencies, performance is instead limited by array aperture. For an array of aperture D, the beamwidth $\Delta\theta$ scales as $\Delta\theta \sim \lambda/D$, so as wavelength increases, the directional response broadens, leading to poor discrimination between incident wave directions [20]. Reliable DOA estimation therefore requires a sufficiently large aperture to produce sufficient phase variation across the sensors [35].

Beamforming is also sensitive to errors in the assumed propagation speed. If the wave speed is over- or underestimated, the steering delays become inaccurate, reducing phase coherence, weakening the main lobe, increasing side-lobe energy, and degrading pinpointing accuracy. Dispersion further worsens these effects by introducing frequency-dependent phase errors [36]. The choice of beamforming weights also matters: uniform weights maximise directivity but increase side-lobe levels, whereas tapered weights suppress side lobes at the cost of a broader main lobe [35]. More advanced adaptive methods such as minimum variance distortionless response (MVDR) [37], multiple signal classification (MUSIC) [38], and estimation of signal parameters via rotational invariant techniques (ESPRIT) [39] can improve interference rejection and DOA estimation, but they depend on reliable covariance or steering-vector estimates and typically incur greater computational cost.

Array geometry further shapes performance. Uniform linear arrays are simple, but provide limited angular coverage, whereas planar and volumetric arrays offer improved spatial resolution and broader coverage at the expense of greater hardware and computational complexity [40]. Signal quality and propagation conditions are also important: higher SNR and strong inter-sensor coherence improve localisation accuracy [19,20], whereas noise, multipath, attenuation, dispersion, and mixed wave types degrade DOA estimates [41,42].

Overall, beamforming effectiveness depends on a trade-off between array design, processing parameters, and operating conditions. Reducing sensor spacing helps suppress aliasing, while increasing aperture improves angular resolution; for a fixed aperture, this generally requires more sensors, with corresponding increases in system complexity and cost. Frequency selection is similarly important: higher frequencies improve angular resolution but increase aliasing risk unless the array spacing is sufficiently small [43], whereas lower frequencies are often more robust to attenuation in lossy media but provide poorer directional discrimination [44]. The optimal frequency band therefore balances attenuation, coherence, noise, and array constraints.

2.4. Leak pinpointing procedures using the seismic camera method

The SCM combines surface vibration measurements with frequency-domain beamforming and iterative array repositioning to pinpoint leaks in buried pipes. It exploits the directional propagation characteristics of the body waves generated by the leak, as described in Section 2.1.

Two operational zones can be distinguished according to the position of the sensor array relative to the leak. In the pipe-oriented zone (POZ), the array is located far from the pipe, and the measured response is dominated by far-field waves radiated from the vibrating pipe; the estimated DOA therefore tends to point towards the pipe axis. In the leak-oriented zone (LOZ), the array is close to the leak or directly above the pipe, and the estimated DOA instead points towards the leak location. The SCM exploits this transition in directional behaviour by first guiding the array towards the pipe alignment and subsequently towards the leak, regardless of the initial array position. The POZ and LOZ are introduced as operational descriptors of these two distinct directional behaviours rather than as spatially fixed regions separated by a universal boundary. The location of the transition depends on propagation conditions, including soil properties, source–structure coupling, measurement geometry, and frequency-dependent attenuation, which determine the relative influence of pipe-guided and leak-radiated wavefields. Consequently, the extent of each regime is expected to vary between installations, and no single quantitative threshold is imposed in the present work.

The SCM employs the beamforming formulation described in Section 2.2 as a core processing step within an iterative pinpointing framework. An array of ground vibration sensors is placed at a given surface location, and signals are recorded simultaneously. The signals may be preprocessed using band-pass filtering to retain frequency components with high inter-sensor coherence and acceptable attenuation. For each selected frequency bin with centre frequency ω_n, the beamformer output is computed using Eq. (6) over a predefined three-dimensional search region. To improve robustness, the outputs are summed across the selected N frequency bins:

$$P_{\text{total}}\left(x_p, y_p, z_p\right) = \sum_{n=1}^{N} P\left(\omega_n, x_p, y_p, z_p\right), \tag{10}$$

thereby reducing frequency-dependent artefacts and enhancing consistent spatial features. The resulting three-dimensional map represents the spatial distribution of coherent energy around the array. Regions of higher power indicate closer proximity to the source. An example of such a map is shown in Fig. 2(a). Rather than directly interpreting the three-dimensional map to estimate source position, the SCM introduces a projection step in which the map is collapsed onto the horizontal plane by averaging over depth:

$$P_{2D}\left(x_p, y_p\right) = \frac{1}{Q}\sum_{q=1}^{Q} P_{\text{total}}\left(x_p, y_p, z_q\right), \tag{11}$$

where Q denotes the number of depth layers. This operation reduces dimensionality and suppresses spurious depth-dependent maxima, while retaining the horizontal localisation information. The depth-averaging interval is selected to encompass the physically relevant region over which the leak-induced wavefield is expected to produce a significant beamformer response. Since the pipe burial depth is generally known approximately from utility records or as-built drawings, the depth projection is not intended to estimate source depth explicitly. Instead, it integrates the beamformer output over a depth range

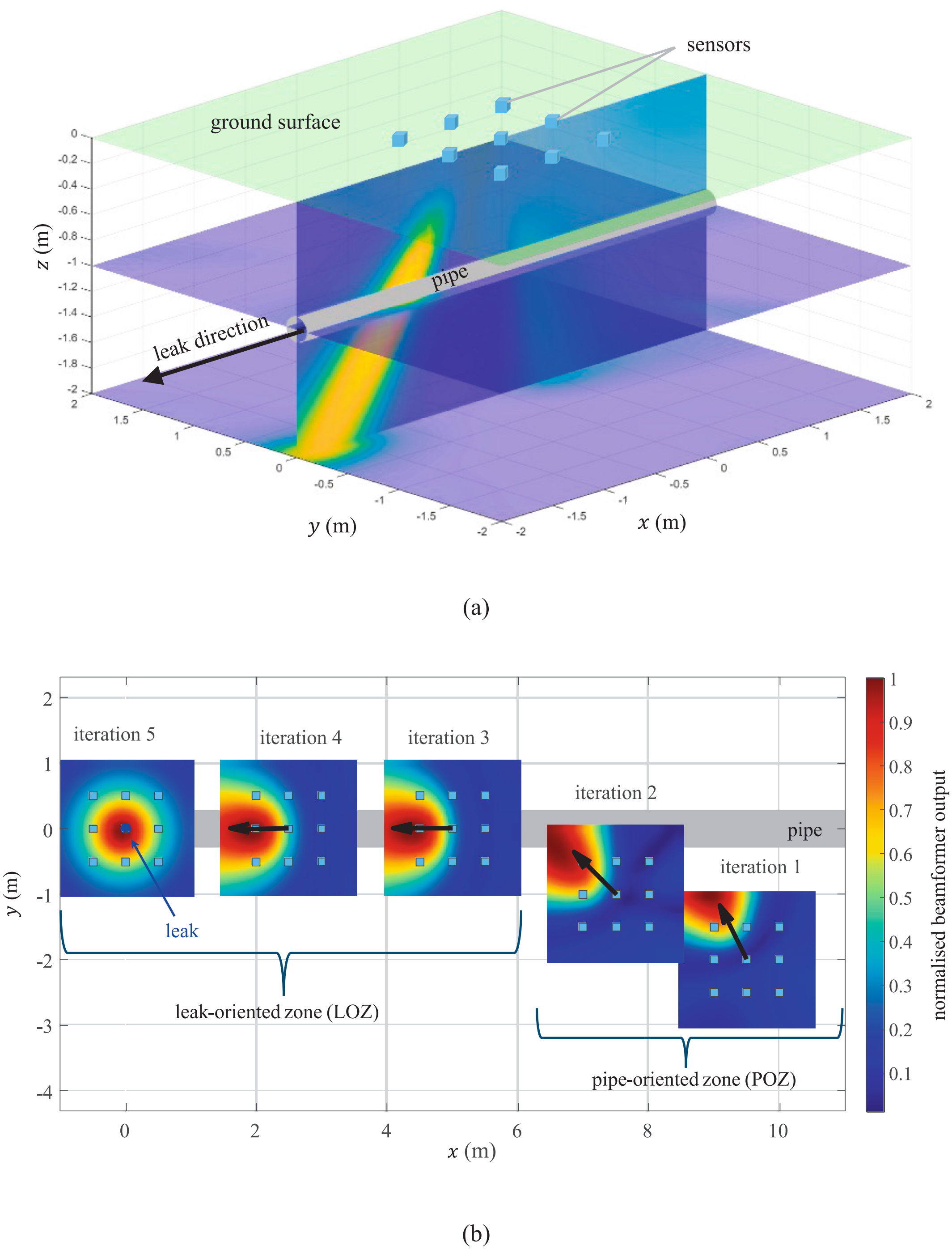

Fig. 2. Illustration of the SCM: (a) three-dimensional beamforming output from seismic measurements above a leaking buried pipe; (b) iterative leak pinpointing.

extending from the ground surface to below the pipe, thereby accommodating modelling uncertainty, finite beamformer resolution, and mode-conversion effects while retaining the dominant leak-related response.

The resulting two-dimensional map P_{2D} is used for localisation: the point of maximum intensity $\left(x_s^{(k)}, y_s^{(k)}\right)$ at iteration k defines the estimated DOA relative to the array centre $\left(x_c^{(k)}, y_c^{(k)}\right)$. If required, the corresponding azimuth angle may be computed using the relation given in Section 2.2. The array is subsequently translated by a predefined step size Δ in the direction of $\left(x_s^{(k)}, y_s^{(k)}\right)$. Signal acquisition, beamforming, and array repositioning are repeated iteratively until the location of maximum intensity lies within a specified tolerance ε of the array centre, i.e.,

$$d^{(k)} = \sqrt{\left(x_s^{(k)} - x_c^{(k)}\right)^2 + \left(y_s^{(k)} - y_c^{(k)}\right)^2} \leq \varepsilon \tag{12}$$

The stopping tolerance may be specified in terms of a permissible angular deviation from the vertical direction corresponding to the array being directly above the leak. For a pipe buried at depth z_{pipe}, an angular tolerance δ corresponds to a horizontal localisation tolerance,

$$\varepsilon = z_{\text{pipe}} \tan(\delta) \tag{13}$$

Smaller values of δ impose stricter convergence requirements and therefore higher localisation precision, whereas larger values reduce the number of iterations at the expense of localisation accuracy. The values of δ and z_{pipe} should be selected according to the requirements of the specific application and are not fixed by the proposed method. For illustration, a maximum angular deviation $\delta = 3^{\circ}$ corresponds to a horizontal tolerance of $\varepsilon = 0.052$ m for a pipe burial depth of 1 m. At convergence, the array centre lies within the prescribed localisation tolerance of the leak position, and the corresponding coordinates are reported. The SCM procedure is summarised in Procedure 1.

Procedure 1. Iterative SCM procedure for leak localisation.

1. **Initialisation**: Place the sensor array at an initial location on the ground surface.
2. **Signal Acquisition**: Measure ground vibrations simultaneously across all sensors.
3. **Beamforming**: Compute beamformer output $\mathrm{P}\left(\omega_{\mathrm{n}}, x_p, y_p, z_p\right)$ using Eq. (6) across selected frequencies ω_{n} at points within the predefined search region around the current array centre.
4. **Frequency Averaging**: Compute $\mathrm{P}_{\text{total}}\left(x_p, y_p, z_p\right)$ using Eq. (10).
5. **Depth averaging:** Compute $\mathrm{P}_{\mathrm{2D}}\left(x_p, y_p\right)$ using Eq. (11).
6. **DOA estimation:** Identify $\left(x_s^{(k)}, y_s^{(k)}\right)$ corresponding to the maximum of $\mathrm{P}_{\mathrm{2D}}\left(x_p, y_p\right)$, and compute (ϕ, θ) if required.
7. **Array Advancement**: Move the array by a predefined step size Δ towards $\left(x_s^{(k)}, y_s^{(k)}\right)$.
8. **Convergence Check**: Compute $d^{(k)} = \sqrt{\left(x_s^{(k)} - x_c^{(k)}\right)^2 + \left(y_s^{(k)} - y_c^{(k)}\right)^2}$. If $d^{(k)} \leq \varepsilon$, terminate; otherwise, return to Step 2.
9. **Output:** Report the leak coordinates.

The iterative behaviour of the SCM is illustrated in Fig. 2(b). When the array is positioned far from the pipe (in the POZ), the beamformer output is dominated by far-field radiation from the pipe, and the estimated DOA guides the array towards the pipe alignment (Iterations 1–2). As the array approaches the pipe or the leak, the response transitions to the LOZ, and the estimated DOA shifts towards the leak location (Iterations 3–5). This transition reflects the underlying wave propagation mechanisms and enables the SCM to converge to the leak location even when the initial array position is remote from the source.

While SCM employs the conventional beamforming formulation described in Section 2.2, its mode of operation differs fundamentally. Conventional beamforming is typically applied as a single-step, fixed-array imaging or DOA estimation technique, where the peak of the beamformer output directly yields the source location. In contrast, the SCM uses beamforming as an intermediate locally applied estimator within an iterative, closed-loop pinpointing framework. The beamformer output is not interpreted as the final source position; instead, it provides a directional cue that guides the progressive movement of the sensor array until convergence at the leak location is achieved. Furthermore, depth averaging combined with array translation converts the problem from static imaging into a dynamic search process. The SCM thus reframes leak pinpointing as an adaptive, iterative procedure that integrates wave propagation behaviour, spatial filtering, and sensor mobility. This enables practical, field-deployable pinpointing using a compact mobile array, without the need for a large, fixed aperture or full-field coverage.

In practical applications, the performance of the SCM depends on several factors. The selected frequency band must balance attenuation and coherence to ensure reliable phase alignment across sensors. The assumed wave speed used in the steering vector must be sufficiently accurate to avoid systematic DOA bias. The array step size must be chosen to ensure stable convergence without excessive iterations or overshooting. In addition, multipath propagation, mode conversion, and mixed wave types may introduce secondary maxima in the beamforming map; the combined use of frequency averaging and depth projection mitigates, but does not entirely eliminate, such effects. In the following section, the SCM is evaluated using numerical simulations and experimental measurements, focusing on the influence of key beamforming parameters on DOA estimation and leak pinpointing.

3. Parametric study of the seismic camera method

The influence of key beamforming parameters—frequency and wave speed—is investigated through numerical simulations using a two-dimensional axisymmetric finite element model of a buried pipe system. This analysis aims to quantify their impact on DOA estimation and leak pinpointing. Noise effects are neglected in this initial study to isolate the intrinsic behaviour of the SCM and demonstrate its feasibility under controlled conditions.

3.1. Numerical simulation setup and procedures

Fig. 3 shows the finite element model of the buried pipe system used to evaluate beamforming performance under varying parameter configurations. The model was implemented in COMSOL Multiphysics v5.2 and comprises three coupled domains: water, pipe, and homogeneous soil. The water domain was modelled as a lossless acoustic medium using the Pressure Acoustics module, while the pipe and soil were represented as linear elastic solids using the Solid Mechanics module. Acoustic–structure interaction at the water–pipe interface was enforced via a coupled boundary condition. Perfectly matched layers (PMLs) were applied at the outer boundaries of the computational domain to suppress artificial reflections and approximate an unbounded soil medium.

The leak was represented as a monopole source positioned at the centre of the pipe, following previous work [10,45]. This source model should be regarded as an idealised benchmark excitation rather than a complete representation of turbulent leakage noise. A monopole source provides a simple and repeatable means of exciting the fluid–pipe–soil system while generating the dominant wave types associated with leak-induced vibration [45]. Although it does not reproduce the full stochastic characteristics of a real leak, it preserves the principal propagation mechanisms, wave speeds, and time-delay relationships that

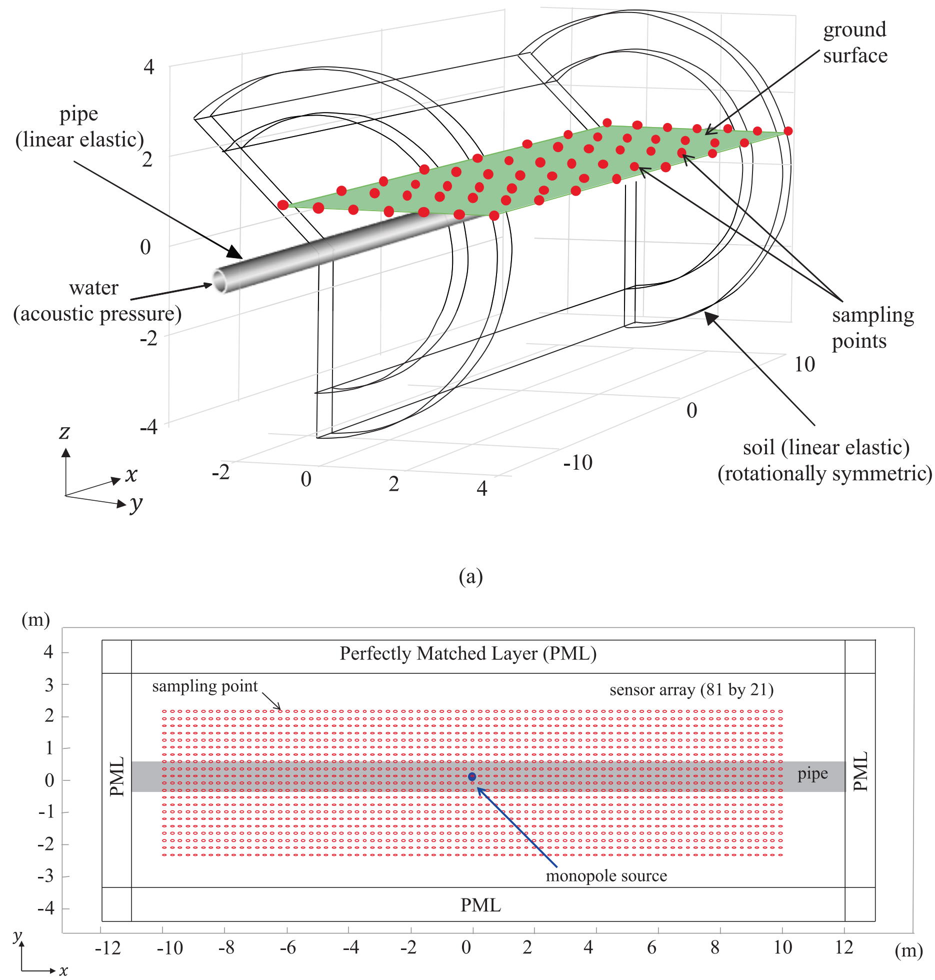

Fig. 3. Schematic of the finite element model. (a) 3D view. (b) Top view. Red dots indicate the points at which the simulated wavefield is sampled.

underpin the beamforming and localisation process. It therefore provides a controlled basis for evaluating the fundamental localisation behaviour of the SCM.

The resulting velocity wavefield, comprising compressional and shear body waves generated by the monopole source, was computed over a frequency range of 50–250 Hz (in increments of 10 Hz). This range encompasses the frequency range at which leak noise is typically dominant in plastic pipes, as reported in experimental studies [46]. The finite element model was discretised using a fine mesh of triangular elements, with the maximum element size set to less than one-sixth of the wavelength at the highest frequency considered.

The simulated wavefield was sampled at discrete points on an 81 × 21 rectangular grid located at the ground surface 1 m above the pipe, with adjacent grid points spaced 0.25 m apart, as illustrated in Fig. 3(b). The surface response used for beamforming was obtained from the axisymmetric finite element model by mapping the rotationally symmetric radial solution onto the Cartesian grid using the radial distance from the pipe axis. Each grid point was assigned the corresponding axisymmetric solution value via interpolation in the radial coordinate. The rectangular grid therefore represents a sampling mesh on the ground plane rather than a full three-dimensional finite element discretisation.

Geometric discontinuities such as bends, joints, and fittings were omitted to preserve the axisymmetric formulation and to isolate the fundamental propagation behaviour of the leak-induced field. This simplification is appropriate for establishing the baseline response of the proposed SCM but limits direct generalisation to complex pipe networks. The influence of wave scattering at structural discontinuities will be considered in future work using fully three-dimensional models and extended experimental validation. The material properties assigned to each domain (Table 1) correspond to those of the MDPE test rig used in the experimental validation presented in Section 4.

Beamforming was performed with a 3 × 3 square array with inter-sensor spacing $d = 0.5$ m. The square geometry was selected because it provides directional sensitivity in both horizontal dimensions while maintaining a compact aperture suitable for iterative repositioning. The

Table 1
Pipe and soil properties in the finite element model [31].

	MDPE Pipe	Soil
Length (m)	20	Infinite
Mean radius (mm)	84.5	–
Wall-thickness (mm)	11	–
Young modulus (GN/m^2)	2	0.128
Shear modulus (MN/m^2)	–	27
Density (kg/m^3)	900	1850
Poisson ratio	0.4	0.3
Loss factor	0.06	0.15
Pipe-borne wave speed (m/s)	375	–
Shear body wave speed (m/s)	–	120
Longitudinal body wave speed (m/s)	–	298

3 × 3 configuration also represents the smallest planar arrangement capable of supporting the local beamforming procedure adopted in this work. Larger apertures, denser spatial sampling, or alternative array geometries could potentially improve angular resolution and robustness to spatial aliasing, but optimisation of the array design is outside the scope of the present proof-of-concept investigation. Because the measured signal contains both shear and compressional waves, the usable frequency band is constrained by both spatial sampling of the two wave types and array aperture considerations. At the upper end, the maximum alias-free frequency is set by the shortest wavelength, corresponding to the shear wave. The half-wavelength criterion, $d \leq \lambda_{\min}/2$, yields $f_{\max} = c_s/(2d) = 120$Hz for the shear-wave component, while the compressional-wave component remains alias-free up to $f_{\max} = c_p/(2d) \approx 298$ Hz. Thus, the shear-wave signal defines the most restrictive upper bound for alias-free beamforming. At the lower end, the finite array aperture limits directional resolution. Sufficient angular discrimination typically requires a phase variation of at least order π across the aperture, $kD \gtrsim \pi$. For the present array with $D = 1$ m, this corresponds to a practical lower frequency bound of $f_{min} \approx c/(2D)$. For shear waves ($c_s = 120$ m/s), this gives $f_{min} = 60$ Hz, whereas for compressional waves ($c_p = 298$ m/s) the lower bound is approximately 150 Hz. Frequencies below these values yield broad, poorly defined DOA estimates. The current inter-sensor spacing of 0.5 m violates the spatial criterion $d \leq \lambda_{\min}/2$, meaning that frequencies above 120 Hz for shear waves and above 298 Hz for compressional waves may exhibit spatial aliasing. Avoiding aliasing across the entire 50–250 Hz simulation band would require $d < 0.24$ m. Nevertheless, the inter-sensor spacing of 0.5 m was retained to maintain consistency with the experimental configuration and practical constraints imposed by the number and size of geophones available for the experimental validation. This choice accepts the risk of aliasing artefacts in favour of experimental reproducibility. Taken together, the most reliable single-frequency beamforming results are obtained in the shear-wave-dominated band of approximately 60–120 Hz. The compressional-wave component remains usable mainly over the higher-frequency portion of the band, approximately 150–250 Hz. However, aliasing and aperture limitations restrict the simultaneous exploitation of both wave types.

The beamforming results are presented in the following subsections. Although they are shown for selected grid points, the observed trends are representative across the entire grid.

3.2. Analysis of direction of arrival estimates

The SCM procedure (Section 2.4) was applied to extract the DOA information at grid points on the ground surface. Beamformer outputs were computed over a square grid centred on the 3 × 3 sensor array, using a frequency of 120 Hz (within the dominant band of the simulated leak noise and free from aliasing) and a beamformer wave speed of 120 m/s. The selected depth interval (0–2 m) spans from the ground surface to 1 m below the pipe axis.

Fig. 4 presents the DOA vectors at interior grid points alongside representative two-dimensional beamformer maps. Each vector points from the array centre in the direction of maximum intensity. Vectors in regions remote from the leak or the pipe generally point towards the pipe, whereas those near the leak or aligned with the pipe axis point

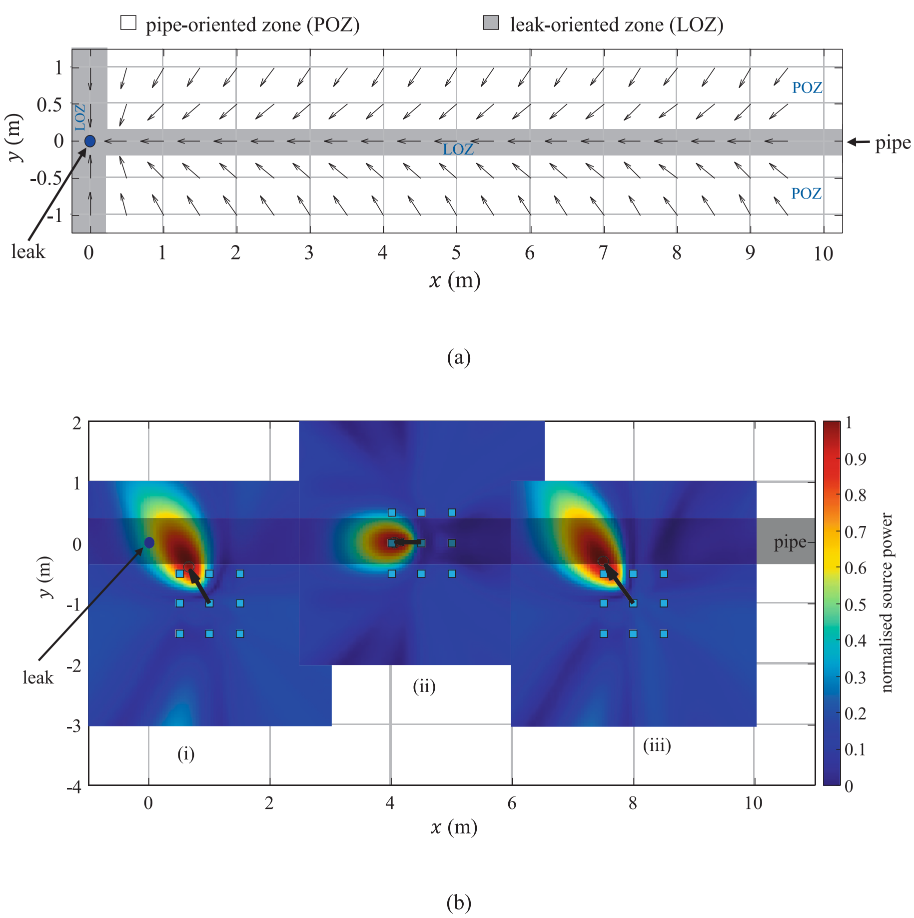

Fig. 4. Estimation of DOA at the ground surface: (a) DOA vectors at the grid points, defined as the direction from the array centre towards the maximum of the beamformer response; (b) representative two-dimensional beamforming maps at selected grid points: (i) $(x, y) = (1.0, -1.0)$ m; (ii) $(x, y) = (4.5, 0)$ m; (iii)$(x, y) = (8.0, -1.0)$ m. The vectors indicate the inferred direction used to guide pinpointing, pointing towards the pipe in the POZ and towards the leak in the LOZ. Beamforming parameters: frequency = 110 Hz; wave speed = 120 m/s.

towards the leak, in agreement with the theoretical predictions in Section 2.1. The DOA angle should not be interpreted as the primary result; the key consideration is whether the inferred direction guides the array towards the pipe in the POZ and towards the leak in the LOZ. In this sense, the method is successful when the back-projected vector remains consistent with the expected search path rather than when it matches a single theoretical incidence angle exactly. The results indicate that the seismic camera provides a physically consistent search direction across the ground surface. These results demonstrate that the seismic camera can reliably pinpoint the leak using ground measurements.

3.3. Effect of frequency on direction-of-arrival estimation

The influence of frequency on DOA estimation was examined at representative grid points located close to the leak, namely $(x, y) = (3, -2)$ and $(7, 1)$ m. Fig. 5 shows the resulting single-frequency DOA estimates over the 50–200 Hz band. Here, the DOA is computed as the angle between the pipe axis and the direction from the array centre to the maximum of the beamformer response. At $(3, -2)$ m, the estimated DOA lies between the theoretical compressional-wave and shear-wave incidence angles over approximately 60–170 Hz when the shear-wave speed is used, and over approximately 60–200 Hz when the compressional-wave speed is used. For $(7, 1)$ m, the corresponding frequency intervals shift to approximately 100–170 Hz and 100–200 Hz, respectively. These results indicate that the beamformer returns a physically meaningful direction only over a limited frequency range in which the leak-generated wavefield is sufficiently coherent and the array aperture provides adequate angular resolution.

This behaviour is consistent with the mixed-mode nature of the simulated leak field. The monopole source generates both compressional and shear body waves, so the observed DOA reflects the dominant apparent propagation direction of the combined field rather than a single pure mode. At low frequencies, the wavelength is large relative to the 3 × 3 array aperture, yielding weak phase variation across the sensors and poor directional discrimination. At higher frequencies, the shear-wave component becomes increasingly vulnerable to spatial aliasing because of the 0.5 m inter-sensor spacing, which promotes grating lobes and destabilises the single-frequency estimate. The intermediate band therefore represents the best compromise between aperture-limited resolution and aliasing, which explains why the DOA remains bounded by the compressional and shear incidence angles over that interval.

The broadband, frequency-summed estimate provides a more stable summary of this behaviour. By combining the beamforming output across the selected frequency band, incoherent artefacts are suppressed and the dominant leak-related direction is recovered more robustly than from any individual frequency bin. As shown in Fig. 5, the summed DOA remains within the angular sector bounded by the compressional- and shear-wave incidence angles and points back towards the pipe. This is consistent with the beamformer map at 200 Hz in Fig. 6(a), where grating lobes obscure the true source direction at a single aliased frequency, whereas frequency summing mitigates these artefacts and yields a more reliable estimate. Frequency summing does not completely eliminate spatial aliasing. Frequency bins above the alias-free limit may still contribute grating-lobe energy; however, their influence is attenuated when combined with lower-frequency components where the spatial sampling is more favourable.

Fig. 6 shows the effect of frequency summing and depth averaging on the simulated beamformer map. At 200 Hz, the single-frequency response is strongly distorted by grating lobes (Fig. 6(a)), whereas summing over 50–200 Hz substantially suppresses these artefacts and yields a clearer pinpointing peak (Fig. 6(b)). In the homogeneous soil model, depth averaging alone has only a negligible effect on the beamformer response (Fig. 6(c)). Consequently, the combined frequency-summed and depth-averaged map (Fig. 6(d)) is only marginally different from the frequency-summed map alone. These

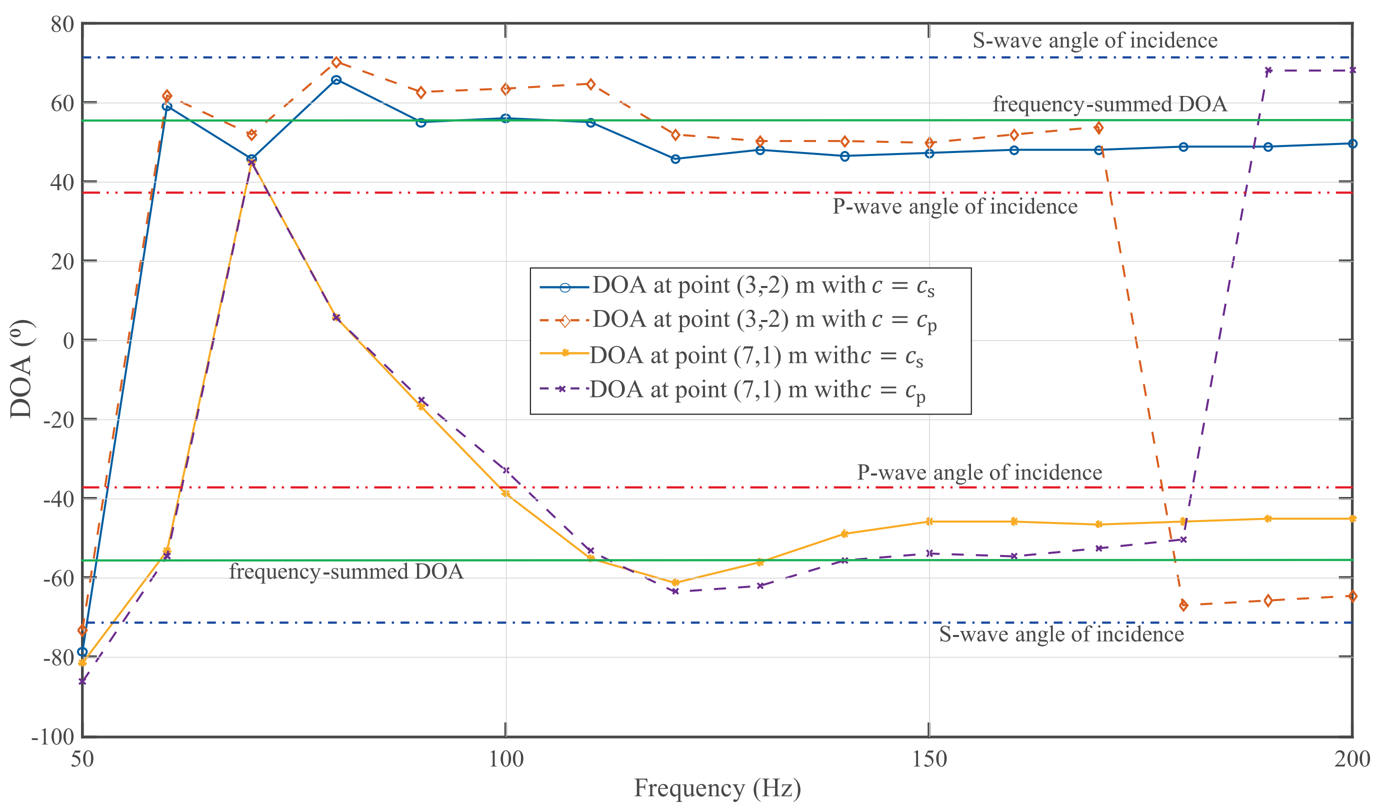

Fig. 5. Frequency dependence of DOA estimation at $(x, y) = (3, -2)$ m and $(x, y) = (7, 1)$ m. Also shown are the P-wave and S-wave incidence angles, and the frequency-summed DOA over the analysed band.

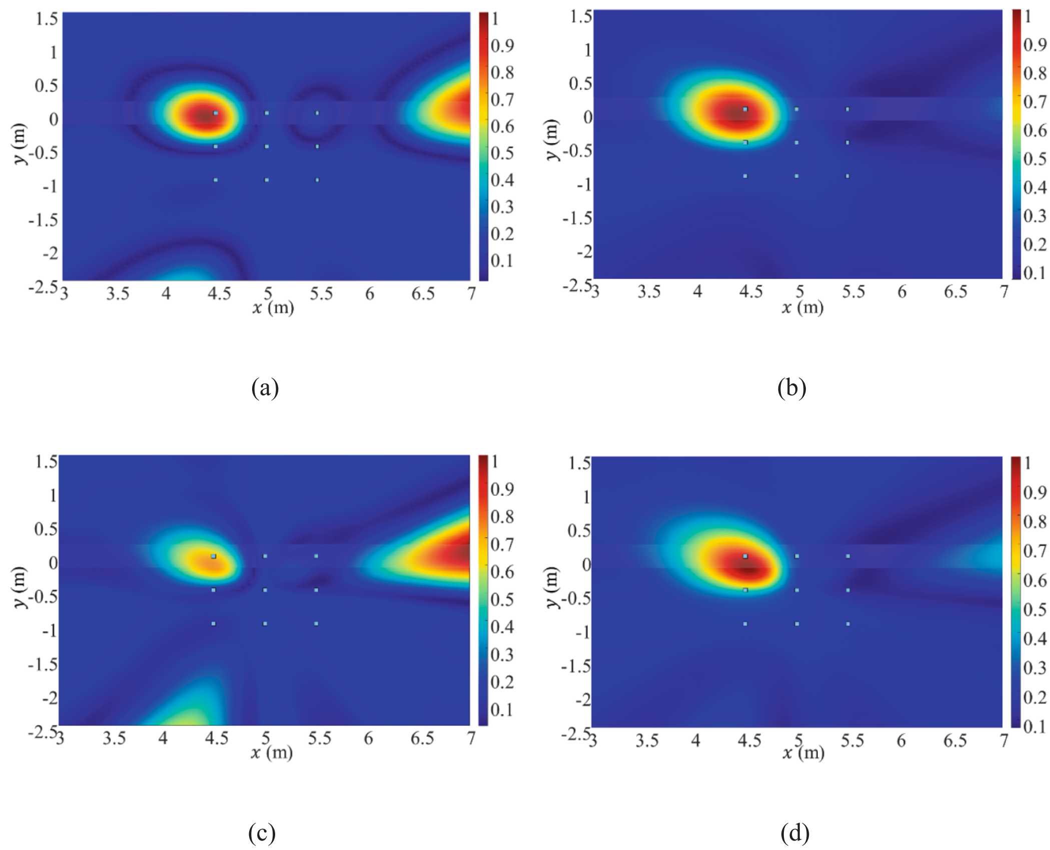

Fig. 6. Effect of frequency summing and depth averaging on the beamformer map at $(x, y) = (5, -0.5)$ m: (a) single-frequency map at 200 Hz and depth 1.5 m; (b) frequency-summed map over 50–200 Hz at depth 1.5 m; (c) single-frequency map at 200 Hz averaged over depths 0–2 m; (d) frequency-summed map over 50–200 Hz and averaged over depths 0–2 m. A wave speed of 120 m/s was used in all cases.

simulation results indicate that frequency summing is the primary mechanism for reducing aliasing artefacts, whereas depth averaging provides little additional benefit in this case.

3.4. Effect of wave speed on direction-of-arrival estimation

Fig. 7 shows the frequency-summed DOA estimates along $y = 1$ m obtained using assumed wave speeds of 120, 298, and 500 m/s. The estimated DOA varies with the assumed wave speed, but the inferred

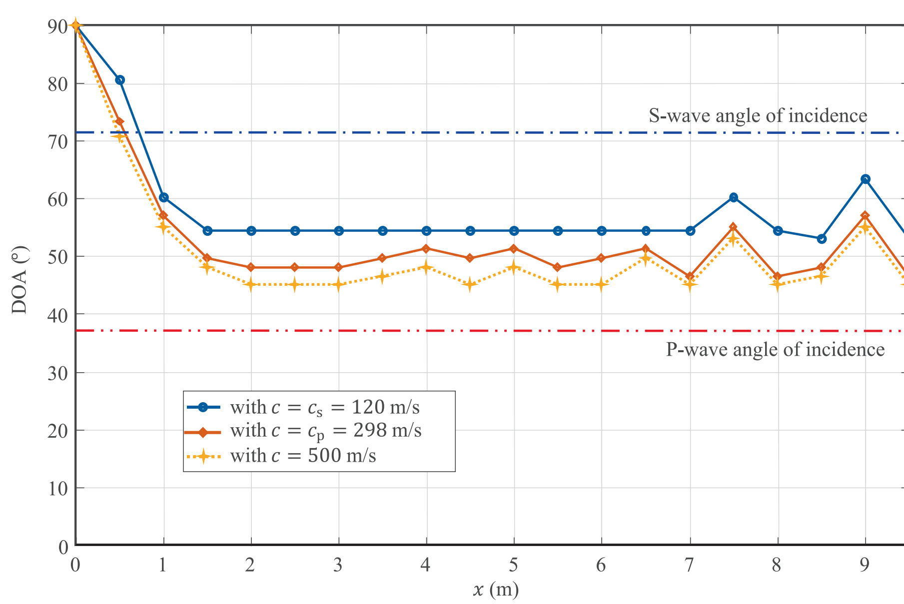

Fig. 7. Effect of assumed wave speed on DOA estimates along $y = 1$ m. Results are shown for assumed wave speeds of 120, 298, and 500 m/s and frequency summing is applied. The reference lines indicate the S- and P-wave incidence angles in the simulated response.

direction remains consistent with the expected path. Near $x_p \to 0$ m, the DOA approaches 90°, consistent with leak pinpointing; farther from the leak, the response shifts into the pipe-oriented regime. In the present geometry, DOA values above about 70° are conservatively regarded as leak-oriented, values below about 60° as pipe-oriented, and intermediate values as transitional. The 120 m/s case is smoother over most of the pipe-oriented region, whereas the 298 and 500 m/s cases are more variable, indicating greater sensitivity to wave speed. The results indicate that the SCM is robust to uncertainty in the assumed wave speed in a limited and well-defined sense. Although changing the assumed speed alters the numerical DOA values and may increase variability, especially away from the leak, the inferred directions remain sufficiently consistent to support iterative leak pinpointing. This reduces the need for accurate site-specific wave-speed calibration, which is often impractical in some field applications.

4. Experimental validation

The beamforming technique and the SCM were validated experimentally using data acquired at a pipe-leak test rig located in Blithfield, United Kingdom [31]. The rig consists of a buried, pressurised MDPE water pipe with an outer diameter of 169 mm and a wall thickness of 11 mm, connected to a vertical standpipe. Leak noise was simulated using a control valve on the standpipe. The resulting pipe motion was monitored using a reference accelerometer (Brüel & Kjær Type 4383) permanently mounted on the pipe surface.

The experimental surface response was acquired using seven I/O SM-24 geophones with 0.5 m spacing, which were deployed sequentially to populate the 32×7 measurement grid shown in Fig. 8. Due to the limited number of available sensors, a full-area simultaneous measurement was not feasible. Nevertheless, since leak-induced vibrations exhibit stationary behaviour under constant operating conditions [47], the surface vibration field was reconstructed through repeated spatial sampling by repositioning the sensor line across successive measurement rows. Each row was recorded at a sampling rate of 1 kHz over a duration of 120 s. To ensure phase consistency across all acquisitions, the pipe-mounted accelerometer was used as a common phase reference. For each grid location, frequency–response functions were estimated relative to the reference signal using the H_1 estimator based on Welch-averaged auto- and cross-spectra [48], with a 1024-sample Hanning window and 50% overlap. The resulting transfer functions were then assembled to reconstruct the cross-spectral matrices required for beamforming. This formulation provides a consistent phase-aligned representation of the spatially sampled wavefield across all measurement rows, despite sequential data acquisition.

The seven geophones are not used as a fixed array for DOA estimation. Instead, they serve as a spatial sampling instrument for reconstructing the ground vibration field over a two-dimensional grid. Directional estimates exploited by the SCM are derived from locally defined beamforming arrays applied at each grid location. Specifically, a 3×3 neighbourhood centred at that point is considered, and the corresponding nine measurement locations are used to construct a local cross-spectral matrix. Beamforming is then applied to this locally defined cross-spectral matrix to obtain a directional estimate associated with that grid point. The result is a spatially distributed field of directional estimates obtained from a sliding-aperture formulation over the measured domain.

Fig. 9 presents the magnitude-squared coherence between the reference leak signal and the geophone signals measured at different grid points. Coherence was estimated using Welch's method with a 1024-point Hann window and 50% overlap, corresponding to a frequency resolution of approximately 1 Hz. Strong coherence is observed in the approximate 50–200 Hz range near the leak, while coherence decreases at higher frequencies (above 120 Hz) and with increasing distance from the source. This indicates that the leak-induced energy is primarily concentrated within this band. For beamforming, the usable frequency range is further constrained by spatial sampling limitations associated with the 0.5 m sensor spacing, as discussed in Section 3.1. In particular, frequencies above approximately 120 Hz may exhibit spatial aliasing; nevertheless, the full coherent band (50–200 Hz) is retained to evaluate the effect of frequency summing. The selected frequency range therefore reflects a deliberate trade-off between signal coherence and spatial sampling constraints, rather than a strictly alias-free regime.

The same SCM procedure used in the numerical study was then applied to the experimental data, with Fig. 10 showing the resulting spatially distributed directional estimates obtained from beamformer evaluations applied to the scanned measurement grid using the sliding 3×3 aperture formulation. As already mentioned, these estimates should be interpreted as locally resolved planar direction indicators derived from a spatially sampled measurement field, rather than as DOA estimates obtained from a single fixed array snapshot. Directional estimates obtained from single-frequency beamformer maps at 110 Hz are compared with those obtained from frequency-summed beamforming over the usable frequency band, using an assumed propagation speed of 120 m/s. The single-frequency results near the aliasing limit exhibit increased variability and occasional directional inconsistencies, whereas frequency summing yields a more stable and spatially coherent directional field. Overall, the experimental results exhibit greater scatter than the numerical simulations, consistent with unmodelled effects such as measurement noise, soil heterogeneity, and limited spatial sampling resolution. Nevertheless, the dominant directional trends are preserved. In the pipe-oriented region, the vectors generally point towards the pipe, while near the leak or directly above the pipe, they converge towards the leak location, in agreement with the numerical results. A small number of local deviations persist in the frequency-summed case; however, these do not disrupt the overall directional consistency or the progression of

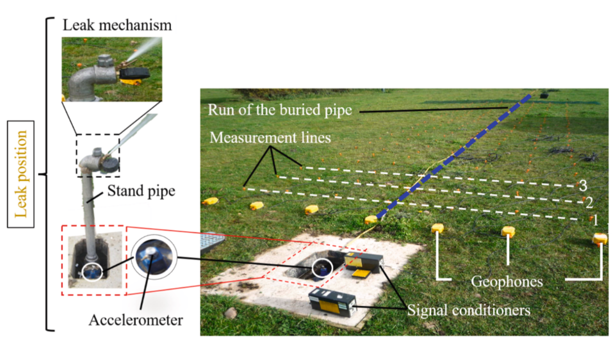

(a)

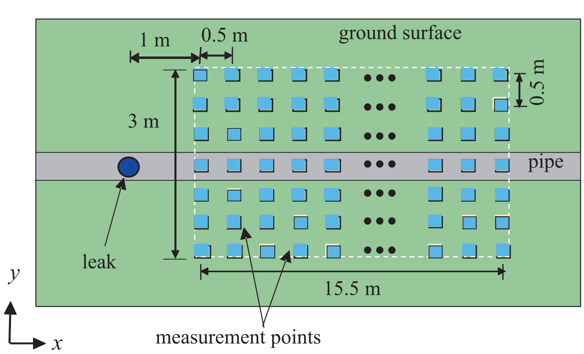

(b)

Fig. 8. Experimental test rig for measuring leak-induced pipe and ground vibrations, showing (a) ground surface instrumentation, including the geophones, the pipe-mounted reference accelerometer, and the leak-generation mechanism; and (b) the plan view of the geophone measurement grid (adapted from [31,49]).

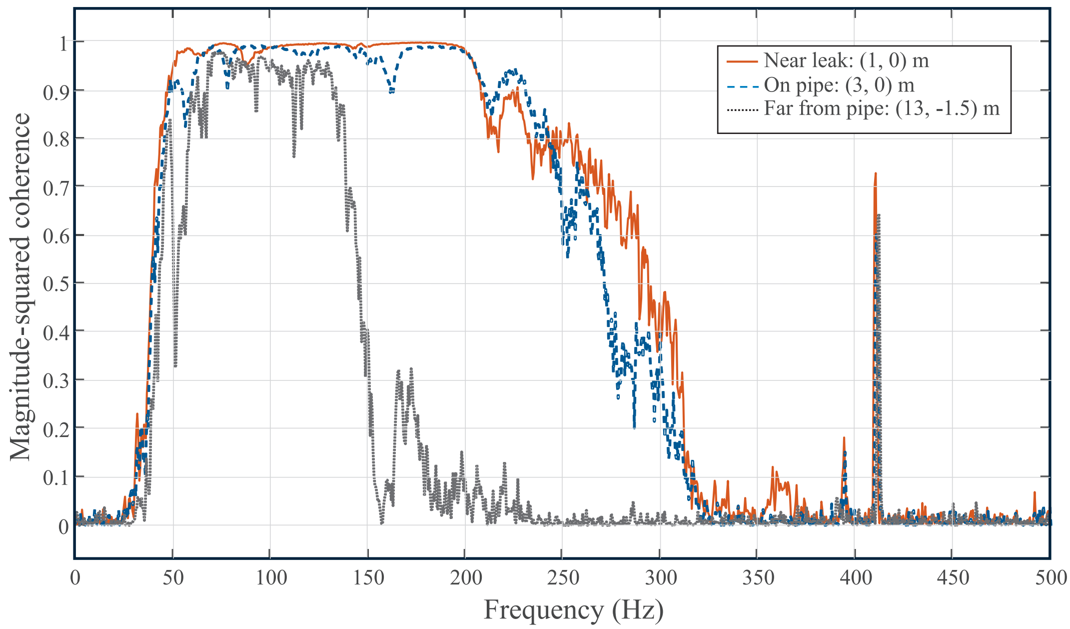

Fig. 9. Representative magnitude-squared coherence between the reference leak signal at $(x, y) = (0, 0)$ m and selected geophone signals. Coherence was estimated using Welch's method with a 1024-point Hann window and 50% overlap.

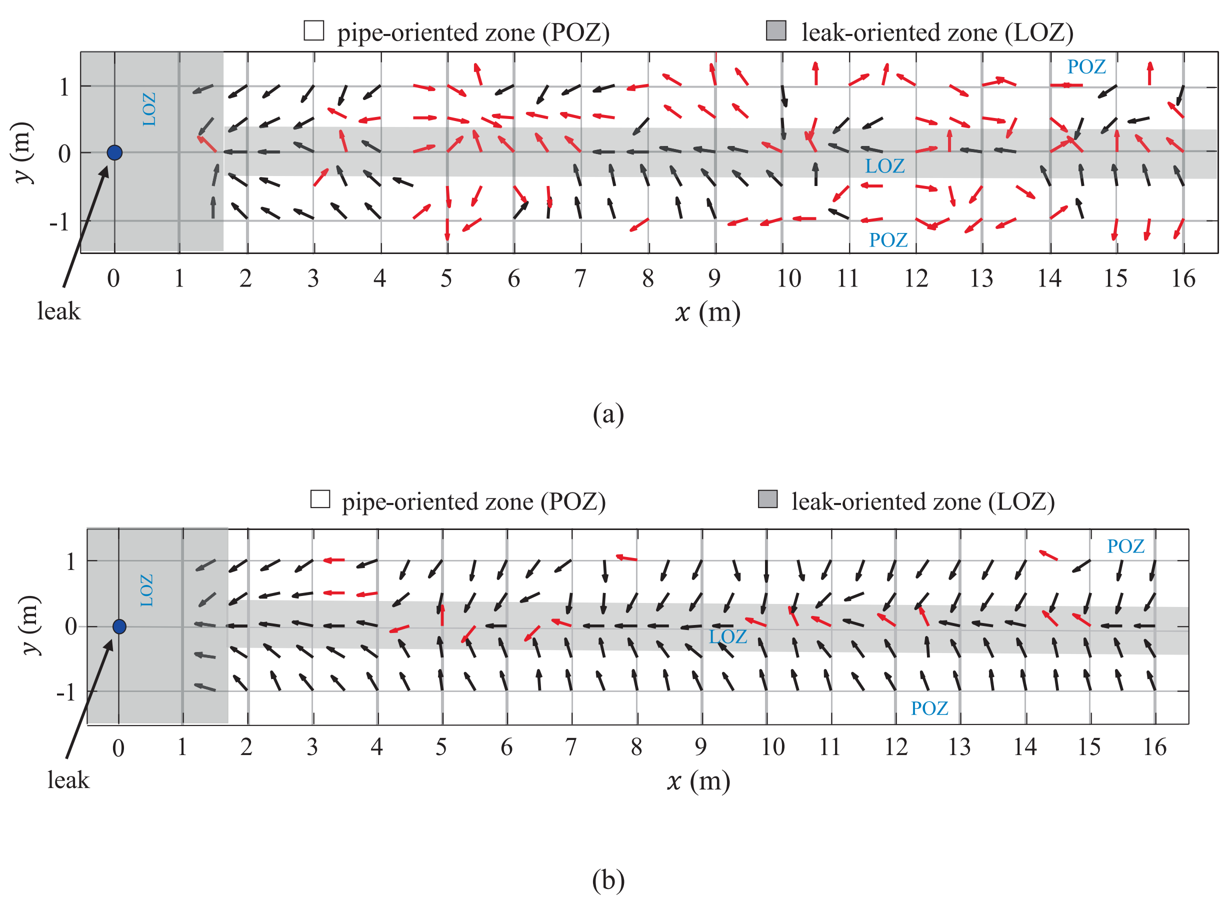

Fig. 10. Spatially distributed planar localisation vectors obtained using a sliding 3×3 aperture over the scanned measurement grid: (a) single-frequency beamformer evaluation at 110 Hz; (b) frequency-summed beamformer evaluation over the usable band. Beamforming assumes a wave speed of 120 m/s. Red vectors indicate locally inconsistent directional estimates relative to the dominant convergence trend towards the leak.

the iterative SCM search towards the leak (see Fig. 14 below).

Figs. 11 and 12 illustrate the effect of frequency summing and depth averaging on the experimental beamformer maps. As in the numerical study, frequency summing provides the primary improvement by suppressing grating-lobe artefacts and sharpening the localisation peak. Depth averaging provides a secondary refinement, with only modest

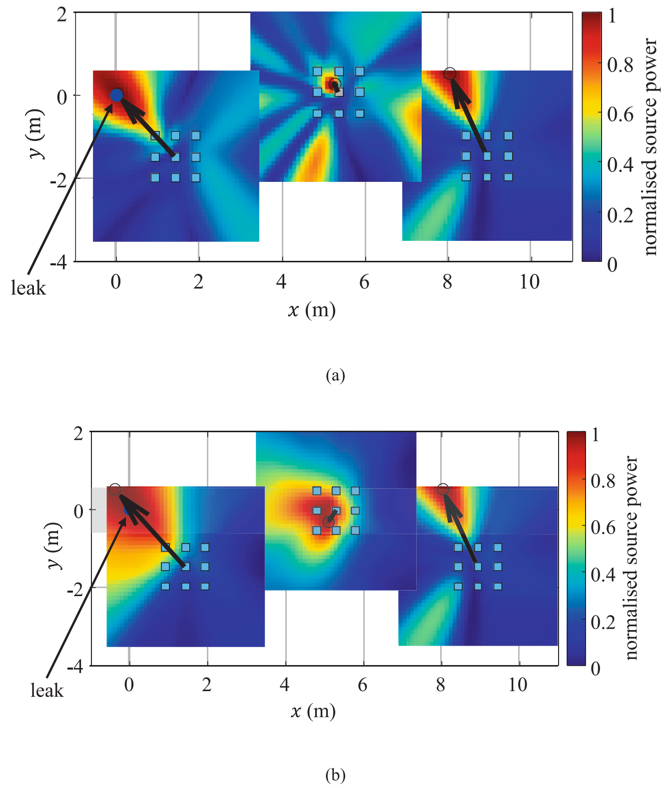

Fig. 11. Effect of frequency summing and depth averaging on the experimental beamformer map: (a) single-frequency maps at 110 Hz at different locations; (b) corresponding frequency-summed maps over the usable band and averaged over depths 0–2 m. A wave speed of 120 m/s was used in all cases.

additional sharpening in selected cases. Overall behaviour is consistent with the simulations.

Fig. 13 examines the influence of assumed wave speed on frequency-summed directional estimates along $y_p = 1$ m. The experimental estimates exhibit greater scatter than the numerical results; however, all three wave-speed cases show broadly consistent directional trends. Across most of the pipe-oriented region, the estimated DOA remains bounded between the P-wave and S-wave incidence angles, indicating mixed-mode propagation behaviour.

Differences in near-field DOA behaviour between simulation and experiment arise from spatial sampling differences. In the simulation, the grid includes the leak location $(x, y) = (0, 0)$, so as $x \to 0$ (with $y = 1$ m), the DOA approaches 90° due to alignment with the vertical. In the experiment, the grid excludes $x = 0$ and begins at $x = 1$ m, so the DOA retains a finite horizontal component and remains below 90°. This difference reflects measurement geometry and grid discretisation rather than beamforming inconsistency.

The results indicate that while the DOA values are sensitive to the assumed wave speed, the relative ordering of directions and their confinement within the expected wave-mode bounds are preserved over most of the domain. The estimated DOA depends on the assumed wave speed, but the directional trend remains consistent, distinguishing between the pipe-oriented and leak-oriented regions.

Finally, the leak-pinpointing capability of the SCM was assessed by replaying the iterative update rule on the pre-acquired measurement grid. Fig. 14 shows the resulting trajectories obtained from multiple starting positions, corresponding to an offline emulation of the SCM iteration using the spatially reconstructed directional field rather than a real-time field deployment in which the physical array is repositioned after each beamforming update. The step size, constrained by the spatial sampling of the measurement grid, is set to 0.5 m in the present implementation. This ensures consistency between the search update and the available measurement resolution. With this constraint, smaller steps would not yield additional spatial information beyond the grid resolution, while larger steps would increase the risk of overshooting the locally inferred direction and producing oscillatory trajectories. Accordingly, the chosen step size is determined by the discretised measurement domain rather than being treated as an optimised continuous parameter.

The trajectories represent movement over the measurement grid driven by locally estimated directions obtained from the sliding-aperture beamforming procedure. In all cases, the trajectories converge to the grid point nearest the leak, $(x, y) = (1, 0)$ m, within 9–35 iterations. Because the leak location does not coincide with a measurement node, the final position is limited by grid resolution rather than beamforming accuracy. Consequently, all trajectories terminate at the same nearest accessible grid point, corresponding to a Euclidean localisation error of 1 m relative to the true leak position. The observed offset from the true leak position reflects a measurement-domain constraint rather than a limitation of the SCM itself. The identical terminal error for all trajectories indicates repeatable convergence of the SCM from the tested starting positions.

Overall, the experimental results broadly corroborate the numerical findings, with frequency summing providing the main improvement and depth averaging offering secondary refinement.

5. Discussion of results

The results indicate that the proposed SCM operates fundamentally as a direction-guided search strategy for leak pinpointing. Rather than relying on precise, point-wise directional estimates, the method exploits the persistence of dominant directional trends within the leak-induced wavefield. Across both the numerical and experimental studies, the estimated directions evolve from alignment towards the pipe in the pipe-oriented region to convergence near the leak itself. Successful leak pinpointing therefore depends on the preservation of this directional structure, which remains robust even under wave-speed mismatch.

The performance of the SCM is governed by the interplay between spatial sampling and frequency selection. Reliable directional estimates are obtained only when the analysed frequencies provide sufficient directional resolution without introducing excessive aliasing. Outside this range, performance deteriorates because of poor angular discrimination at low frequencies and grating-lobe artefacts at high frequencies. Consequently, successful application of the SCM depends on selecting a frequency band that is appropriate for the array geometry, as discussed in Section 2.3. Frequency summing plays a critical role in improving robustness by reinforcing directional features that persist across frequency bins while suppressing frequency-dependent inconsistencies and artefacts. By contrast, depth averaging provides only a modest additional refinement by suppressing spurious depth-related maxima within the three-dimensional beamformer map.

Several simplifying assumptions were adopted to isolate the core localisation mechanism, including a homogeneous soil medium, a single leak source, and an idealised pipe geometry without structural discontinuities. These assumptions provide a controlled baseline for evaluating the SCM, but do not capture the full complexity of operational pipe networks, as the present study is intended as a proof of concept. Nevertheless, both numerical and experimental results exhibit consistent localisation behaviour, indicating that the directional-search mechanism remains effective under realistic conditions. Although experimental measurements are affected by noise, soil variability, and finite spatial sampling, the dominant directional structure of the leak-induced field is sufficiently preserved to guide the iterative search towards the leak. The observed robustness under moderate wave-speed mismatch further suggests that exact site-specific calibration is not strictly required for effective operation. To delineate the applicability limits under more complex field conditions, future work should investigate layered or heterogeneous soils, multiple simultaneous leaks, more

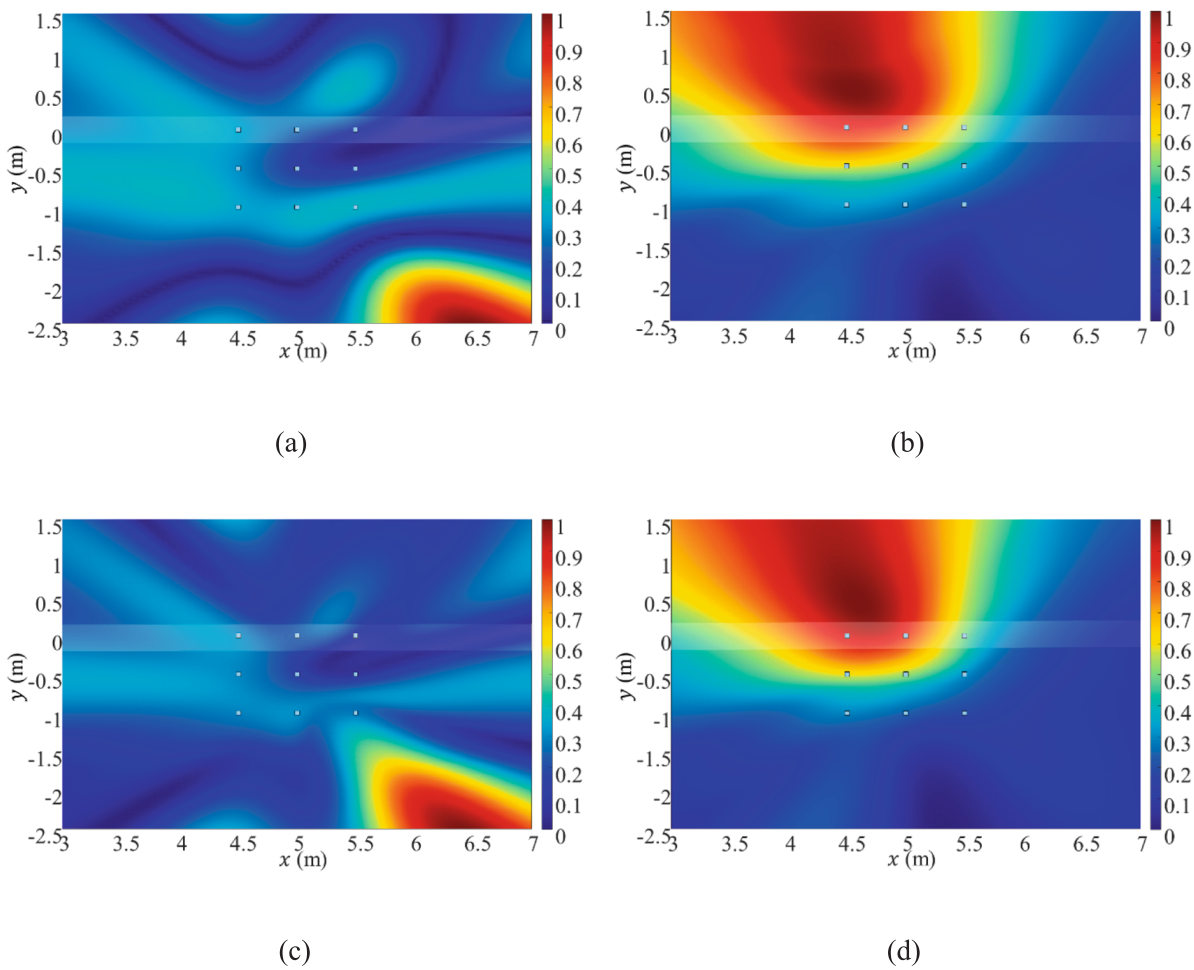

Fig. 12. Effect of frequency summing and depth averaging on the beamformer map at $(x, y) = (5, -0.5)$ m: (a) single-frequency map at 110 Hz and depth 1.5 m; (b) frequency-summed map over 50–200 Hz at depth 1.5 m; (c) single-frequency map at 110 Hz averaged over depths 0–2 m; (d) frequency-summed map over 50–200 Hz and averaged over depths 0–2 m. A wave speed of 120 m/s was used in all cases.

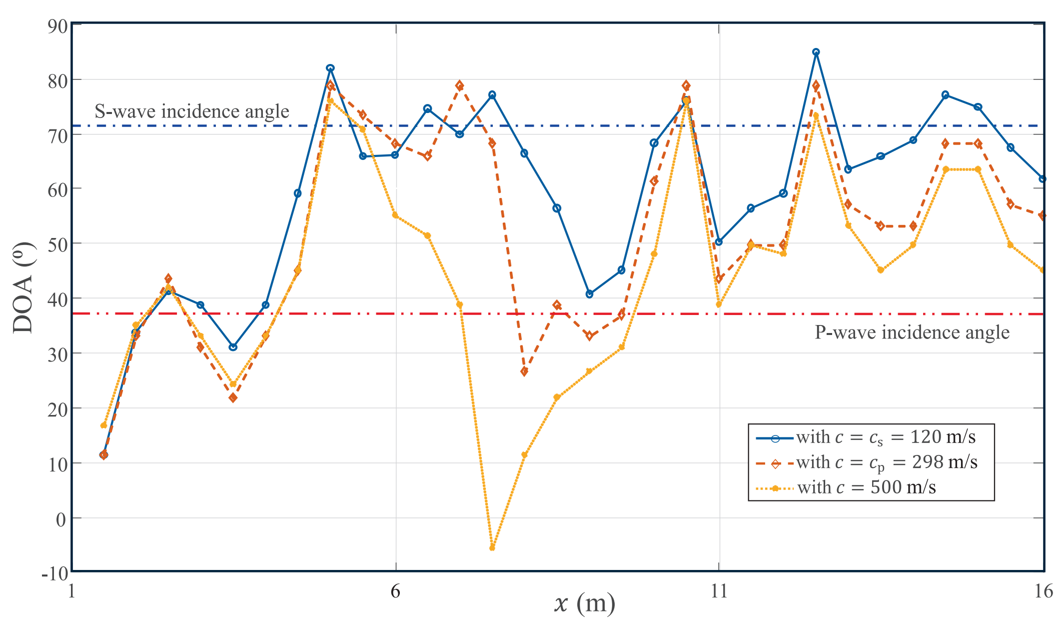

Fig. 13. Effect of assumed wave speed on experimental directional estimates along $y = 1$ m, shown for 120, 298, and 500 m/s with frequency summing.

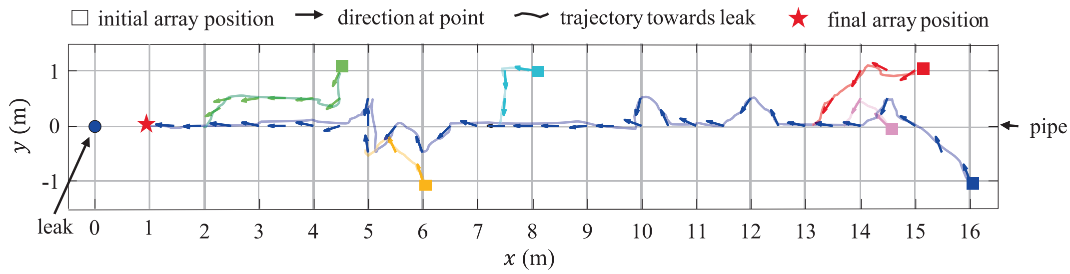

Fig. 14. Offline replay of SCM-based localisation trajectories over the scanned measurement grid. Each trajectory is driven by locally estimated directional fields obtained from the sliding 3×3 beamforming procedure. The step size is 0.5 m. Trajectories converge to the grid point nearest the leak, $(x, y) = (1, 0)$ m. The path trace for each starting point is colour coded.

realistic leakage excitation mechanisms, and wave scattering from structural discontinuities, which are also challenges encountered by other vibro-acoustic leak-detection techniques.

From a practical perspective, the SCM differs from conventional leak pinpointing methods in its measurement strategy and deployment paradigm. Acoustic correlation estimates leak position from time-delay information between sensors installed at known pipe locations and typically requires multiple access points. Its performance can degrade in plastic distribution networks due to strong attenuation of high-frequency components, and in cases where the distance between accessible points exceeds the effective propagation range of leak-induced signals. By contrast, the SCM relies on ground-surface vibration measurements and allows the sensing array to be repositioned dynamically along the suspected asset corridor, thereby bypassing the constraints imposed by sparse pipe access infrastructure. In addition, whereas conventional acoustic listening surveys rely on a single sensor and local signal amplitude, the SCM exploits spatial phase information across a geophone array through beamforming. This phase-based approach offers superior robustness as noted by Muggleton et al. [50] in the context of leak detection via phase unwrapping.

Overall, the results indicate that leak localisation can be effectively formulated as an iterative directional-search problem governed by the spatial coherence of the leak-induced wavefield. Within this framework, the combination of local beamforming and iterative array repositioning provides a consistent mechanism for progressively refining the estimated leak direction using surface vibration measurements. The present study therefore establishes the feasibility of this approach and clarifies the key factors that influence its performance.

6. Conclusions

This study presented the seismic camera method (SCM) as a novel, non-invasive framework for pinpointing leaks in buried pipes using surface vibration measurements. The method integrates frequency-domain beamforming, depth projection, and iterative array repositioning to pinpoint leaks without direct pipe access. The SCM operates by exploiting the directional structure of the leak-induced wavefield to guide an iterative search towards the leak location. The experimental results reproduce the key directional and localisation behaviours predicted by the simplified numerical model, indicating that the underlying SCM mechanism persists beyond the idealised simulation assumptions. Performance is enhanced by frequency summing, which improves the stability and consistency of the estimated directions, while depth averaging provides a smaller secondary refinement. Across both simulation and experiment, successful pinpointing is governed primarily by the preservation of dominant directional trends in the wavefield rather than by precise point-wise direction estimates. The method further exhibits robustness to moderate wave-speed mismatch, indicating tolerance to uncertainty in propagation conditions. Overall, the findings confirm the feasibility of local beamforming combined with iterative repositioning as a leak-pinpointing strategy for buried pipelines, particularly where direct pipe access is restricted. Future work will consider more realistic conditions, including heterogeneous soils, multiple leaks, structural discontinuities, and more complex leakage sources, alongside improvements in array design, adaptive processing, and depth estimation to enhance practical performance.

CRediT authorship contribution statement

P.H.M.C. Matos: Writing – original draft, Formal analysis, Data curation, Conceptualization. **N. Uchendu:** Writing – review & editing, Writing – original draft, Visualization, Validation, Methodology, Investigation, Formal analysis, Data curation, Conceptualization. **F.C.L. Almeida:** Data curation, Resources, Supervision, Writing – original draft. **M.J. Brennan:** Writing – review & editing, Supervision. **B.C. Campos:** Investigation, Validation. **M. Karimi:** Data curation. **J.M. Muggleton:** Data curation. **E. Rustighi:** Writing – review & editing, Writing – original draft, Supervision, Resources, Project administration, Methodology, Investigation, Funding acquisition, Formal analysis, Data curation, Conceptualization.

Declaration of competing interest

The authors declare that they have no known competing financial interests or personal relationships that could have appeared to influence the work reported in this paper.

Acknowledgements

This work was financially supported by: (i) Fondazione CARITRO in the framework of the project E63C24001520003 Seismic camera and digital-twin for water loss detection; (ii) European Union's Horizon 2020 research and innovation programme under Grant Agreement 101016888 (iii) the São Paulo Research Foundation (FAPESP) under Grant numbers 2022/12251-1 and 2022/07586-0.

Data availability

Data will be made available on request.

References

[1] Liemberger R, Wyatt A. Quantifying the global non-revenue water problem. Water Supply 2018;19(3):831–7. https://doi.org/10.2166/ws.2018.129.
[2] Hu Z, Tariq S, Zayed T. A comprehensive review of acoustic based leak localization method in pressurized pipelines. Mech Syst Sig Process 2021;161:107994. https://doi.org/10.1016/j.ymssp.2021.107994.
[3] Colombo AF, Lee P, Karney BW. A selective literature review of transient-based leak detection methods. J Hydro Environ Res 2009;2(4):212–27. https://doi.org/10.1016/j.jher.2009.02.003.
[4] Murvay P-S, Silea I. A survey on gas leak detection and localization techniques. J Loss Prev Process Ind 2012;25(6):966–73. https://doi.org/10.1016/j.jlp.2012.05.010.
[5] Brennan MJ, et al. Achieving zero leakage by 2050: detection and location methods acoustic leak detection. 2017, London, United Kingdom: UK Water Industry Research (UKWIR). ISBN: 1 84057 836 X.

[6] Farrow J, et al. Achieving zero leakage By 2050: the basic mechanisms of bursts and leakage. 2017, London, UK: UK Water Industry Research (UKWIR). ISBN: 1 84057 835 1.
[7] Muggleton JM, Brennan MJ, Pinnington RJ. Wavenumber prediction of waves in buried pipes for water leak detection. J Sound Vib 2002;249(5):939–54. https://doi.org/10.1006/jsvi.2001.3881.
[8] Muggleton JM, Brennan MJ, Linford PW. Axisymmetric wave propagation in fluid-filled pipes: wavenumber measurements in in-vacuo and buried pipes. J Sound Vib 2004;270(1–2):171–90. https://doi.org/10.1016/S0022-460X(03)00489-9.
[9] Almeida F, et al. On the acoustic filtering of the pipe and sensor in a buried plastic water pipe and its effect on leak detection: an experimental investigation. Sensors 2014;14(3):5595–610. https://doi.org/10.3390/s140305595.
[10] Brennan MJ, et al. On the effects of soil properties on leak noise propagation in plastic water distribution pipes. J Sound Vib 2018;427:120–33. https://doi.org/10.1016/j.jsv.2018.03.027.
[11] Almeida FCL, et al. On the signum function and its effect on acoustic correlation for leak location in buried plastic water pipes. Procedia Eng 2017;199:1344–9. https://doi.org/10.1016/j.proeng.2017.09.346.
[12] Gao Y, et al. Application of the differentiation process into the correlation-based leak detection in urban pipeline networks. Mech Syst Sig Process 2018;112: 251–64. https://doi.org/10.1016/j.ymssp.2018.04.036.
[13] Uchendu N, Muggleton JM, White PR. Wavelet-based and data-adaptive methods for time delay estimation in acoustic leak detection. Mech Syst Sig Process 2024; 221:111727. https://doi.org/10.1016/j.ymssp.2024.111727.
[14] Uchendu N, Muggleton JM, White PR. Cepstral method for time delay estimation in acoustic leak detection. Mech Syst Sig Process 2025;241:113448. https://doi.org/10.1016/j.ymssp.2025.113448.
[15] Uchendu N, Muggleton JM, White PR. Cross-spectral phase method for time delay estimation in acoustic leak detection. Appl Acoust 2025;235:110695. https://doi.org/10.1016/j.apacoust.2025.110695.
[16] Uchendu N, Muggleton JM, White PR. Acoustic leak localisation based on multipath identification. J Sound Vib 2025;602:118970. https://doi.org/10.1016/j.jsv.2025.118970.
[17] Jette AN, Parker JG. Surface displacements accompanying the propagation of acoustic waves within an underground pipe. J Sound Vib 1980;69(2):265–74. https://doi.org/10.1016/0022-460X(80)90611-2.
[18] Muggleton J, Gao Y, Brennan M. Vibration radiation from buried plastic water pipes: an experimental investigation at the ground surface. in International Conference on Noise & Vibration Engineering (ISMA) (15/09/12 - 17/09/12). 2012. https://past.isma-isaac.be/downloads/isma2012/papers/isma2012_0600.pdf.
[19] Johnson DH, Dudgeon DE. Array signal processing: concepts and techniques. Prentice-Hall signal processing series. 1993, Englewood Cliffs, NJ: P T R Prentice Hall.
[20] Van Trees HL. Optimum array processing: part IV of detection, estimation, and modulation theory. 2004: Wiley.
[21] McLaskey GC, Glaser SD, Grosse CU. Beamforming array techniques for acoustic emission monitoring of large concrete structures. J Sound Vib 2010;329(12): 2384–94. https://doi.org/10.1016/j.jsv.2009.08.037.
[22] Cui X, et al. Performance comparison of acoustic emission sensor arrays in different topologies for the localization of gas leakage on a flat-surface structure. Sens Actuators, A 2019;300:111659. https://doi.org/10.1016/j.sna.2019.111659.
[23] Zheng X, et al. A beamforming-based joint estimation method for gas pipeline leak localization. Measurement 2021;177:109264. https://doi.org/10.1016/j.measurement.2021.109264.
[24] Gao Y, et al. An analytical model of ground surface vibration due to axisymmetric wave motion in buried fluid-filled pipes. J Sound Vib 2017;395. https://doi.org/10.1016/j.jsv.2017.02.022. p. 142–159-142–159.
[25] Wang T, Wang X, Hong M. Gas leak location detection based on data fusion with time difference of arrival and energy decay using an ultrasonic sensor array. Sensors 2018;18(9):2985. https://doi.org/10.3390/s18092985.
[26] Matos PC, et al. Preliminary numerical simulation for the development of a seismic camera. In: Recent Trends in Wave Mechanics and Vibrations. Springer International Publishing; 2023. https://doi.org/10.1007/978-3-031-15758-5_112.
[27] Castellini P, Sassaroli A. Acoustic source localization in a reverberant environment by average beamforming. Mech Syst Sig Process 2010;24(3):796–808. https://doi.org/10.1016/j.ymssp.2009.10.021.
[28] Choi Y-C, Kim Y-H. Near field impulsive source localization in a noisy environment. J Sound Vib 2007;303(1–2):209–20. https://doi.org/10.1016/j.jsv.2007.01.024.
[29] Ewing WM. Elastic waves in layered media. 1957: McGraw-Hill.
[30] Jette AN, Parker JG. Excitation of an elastic half-space by a buried line source of conical waves. J Sound Vib 1979;67(4):523–31. https://doi.org/10.1016/0022-460X(79)90443-7.
[31] Scussel O, et al. Analysis of phase data from ground vibration measurements above a leaking plastic water pipe. J Sound Vib 2023:117873. https://doi.org/10.1016/j.jsv.2023.117873.
[32] Chiariotti P, Martarelli M, Castellini P. Acoustic beamforming for noise source localization – reviews, methodology and applications. Mech Syst Signal Pr 2019; 120:422–48. https://doi.org/10.1016/j.ymssp.2018.09.019.
[33] Leclère Q, et al. A unified formalism for acoustic imaging based on microphone array measurements. Int J Aeroacoust 2017;16(4–5):431–56. https://doi.org/10.1177/1475472X17718883.
[34] Dougherty RP. Beamforming in acoustic testing, in aeroacoustic measurements, T. J. Mueller, Editor. 2002, Springer Berlin Heidelberg: Berlin, Heidelberg. p. 62-97. https://doi.org/10.1007/978-3-662-05058-3_2.
[35] Merino-Martínez R, et al. A review of acoustic imaging methods using phased microphone arrays. CEAS Aeronaut J 2019;10(1):197–230. https://doi.org/10.1007/s13272-019-00383-4.
[36] Rost S, Thomas C. Array seismology: methods and applications. Rev Geophys 2002; 40(3). https://doi.org/10.1029/2000RG000100. pp. 2–1-2-27.
[37] Capon J. High-resolution frequency-wavenumber spectrum analysis. Proc IEEE 1969;57(8):1408–18. https://doi.org/10.1109/PROC.1969.7278.
[38] Schmidt R. Multiple emitter location and signal parameter estimation. IEEE Trans Antennas Propag 1986;34(3):276–80. https://doi.org/10.1109/TAP.1986.1143830.
[39] Roy R, Kailath T. ESPRIT-estimation of signal parameters via rotational invariance techniques. IEEE Trans Acoust Speech Signal Process 1989;37(7):984–95. https://doi.org/10.1109/29.32276.
[40] Burrus CS, Pillai SU. Array signal processing. New York: Springer; 2012.
[41] Krim H, Viberg M. Two decades of array signal processing research: the parametric approach. IEEE Signal Process Mag 1996;13(4):67–94. https://doi.org/10.1109/79.526899.
[42] Stoica P, Nehorai A. MUSIC, maximum likelihood, and Cramer-Rao bound. IEEE Trans Acoust Speech Signal Process 1989;37:720–41. https://doi.org/10.1109/29.17564.
[43] Ward DB, Kennedy RA, Williamson RC. Theory and design of broadband sensor arrays with frequency invariant far-field beam patterns. J Acoust Soc Am 1995;97 (2):1023–34. https://doi.org/10.1121/1.412215.
[44] Cox H, Zeskind R, Owen M. Robust adaptive beamforming. IEEE Trans Acoust Speech Signal Process 1987;35(10):1365–76. https://doi.org/10.1109/TASSP.1987.1165054.
[45] Quartaroli MM, et al. On the excitation of the Korteweg and Lamb waves in plastic water pipes by leak noise: historical perspective, experimental observation and physical insight. J Sound Vib 2026:119929. https://doi.org/10.1016/j.jsv.2026.119929.
[46] Hunaidi O, Chu WT. Acoustical characteristics of leak signals in plastic water distribution pipes. Appl Acoust 1999;58(3):235–54. https://doi.org/10.1016/S0003-682X(99)00013-4.
[47] Papastefanou AS, Joseph PF, Brennan MJ. Experimental investigation into the characteristics of in-pipe leak noise in plastic water filled pipes. Acta Acust Acust 2012;98(6):847–56. https://doi.org/10.3813/AAA.918568.
[48] Bendat JS, Piersol AG. Random data. Wiley Series in Probability and Statistics. 2010: Wiley.
[49] Iwanaga MK, et al. A technique to pinpoint a leak in a buried water pipe using a pair of roving sensors measuring ground surface vibration. Appl Acoust 2026;243: 111094. https://doi.org/10.1016/j.apacoust.2025.111094.
[50] Muggleton JM, Brennan MJ, Gao Y. Determining the location of buried plastic water pipes from measurements of ground surface vibration. J Appl Geophys 2011; 75(1):54–61. https://doi.org/10.1016/j.jappgeo.2011.06.030.